Journal of Power Sources 409 (2019) 94–101

Contents lists available at ScienceDirect

Journal of Power Sources

journal homepage: www.elsevier.com/locate/jpowsour

# A theoretical study on the stability and ionic conductivity of the $Na_{11}M_2PS_{12}$ (M = Sn, Ge) superionic conductors

Jiapeng Liu[a], Ziheng Lu[a], Mohammed B. Effat[a], Francesco Ciucci[a,b,*]

[a] Department of Mechanical and Aerospace Engineering, The Hong Kong University of Science and Technology, Hong Kong China
[b] Department of Chemical and Biological Engineering, The Hong Kong University of Science and Technology, Hong Kong China

## HIGHLIGHTS

- Superionic conductors $Na_{11}M_2PS_{12}$ (M = Sn, Ge) have been investigated using DFT.
- $Na_{11}Ge_2PS_{12}$ is predicted to be more stable than $Na_{11}Sn_2PS_{12}$.
- Substitution of Sn with Ge increases the bandgap and improves the Na conductivity.
- $Na_{11}Ge_2PS_{12}$ shows the highest RT ionic conductivity in the Na-Ge-P-S family.
- Two types of Na diffusion mechanism in $Na_{11}Ge_2PS_{12}$ have been discovered.

## ARTICLE INFO

*Keywords:*
Solid-state superionic conductors
Sodium sulfur batteries
Density functional theory
ab-initio molecular dynamics

## ABSTRACT

The search for next-generation solid-state superionic conductors has attracted significant attention. Among Na superionic conductors, $Na_{11}Sn_2PS_{12}$ has been reported to have a room temperature ionic conductivity of 1.4 mS/cm. In this study, we employ density functional theory to study the stability of $Na_{11}Sn_2PS_{12}$ and further explore the substitution of Sn with Ge. Our results indicate that $Na_{11}Ge_2PS_{12}$ is more stable than $Na_{11}Sn_2PS_{12}$. Furthermore, substituting Sn with Ge increases the band gap, improves the room temperature ionic conductivity by a factor of 2, and lowers the activation energy of Na hopping. Statistical analysis suggests that $Na_{11}Ge_2PS_{12}$ has a faster diffusion along the *ab*-plane compared to the *c*-axis. The Na diffusion in $Na_{11}Ge_2PS_{12}$ appears to occur with two different mechanisms depending on temperature: 1) an ion hopping process at lower temperatures (< 800 K); 2) a fluid-like distribution of Na ions at higher temperatures (> 1000 K). The computations suggest that $Na_{11}Ge_2PS_{12}$ is a promising candidate as a solid Na electrolyte due to its high room temperature ionic conductivity and phase stability. In light of these simulation results, we expect to stimulate further experimental studies on $Na_{11}Ge_2PS_{12}$.

## 1. Introduction

Rechargeable lithium-ion batteries (LIBs), are critical components of portable electronic devices, electric vehicles, and sustainable energy storage systems. However, LIBs are expensive, and Li is scarce. These shortcomings have triggered a worldwide search for alternative technologies [1–7]. Sodium-ion batteries (SIBs) [8–11] are particularly promising because Na is far more abundant than Li. Additionally, in contrast to LIBs, the most promising cathode materials for SIBs are Co free [10,11]. Avoiding Co helps lower the costs. However, similar to conventional LIB technology, SIBs are intrinsically unsafe because the most commonly used liquid organic electrolytes are flammable and corrosive [12]. Employing solid-state electrolytes (SSEs) would circumvent these challenges as SSEs are generally safer [13–16].

Among recently discovered SSEs, sulfide-based Na ionic conductors have attracted a great deal of attention due to their relatively high ionic conductivity [9,17–23]. One of the most significant milestones in this area is the discovery of cubic $Na_3PS_4$, a material with a Na conductivity of 0.2 mS/cm at room temperature (RT) [18]. Later improvements enabled an enhancement in the ionic conductivity up to 1.2 mS/cm by replacing S in $Na_3PS_4$ with Se to obtain $Na_3PSe_4$ [24]. Inspired by $Li_{10}GeP_2S_{12}$ (LGPS) [25], a state-of-the-art lithium superionic conductor [25–28], Kandagal et al. studied the Na diffusional properties in $Na_{10}GeP_2S_{12}$ and predicted its RT ionic conductivity, $\sigma_{Na}$, to be 4.7 mS/cm [29]. Such a value is particularly encouraging because it is much higher than those reported for all other known Na superionic

* Corresponding author. Department of Chemical and Biological Engineering, The Hong Kong University of Science and Technology, Hong Kong China.
*E-mail address:* mefrank@ust.hk (F. Ciucci).

https://doi.org/10.1016/j.jpowsour.2018.10.077
Received 27 September 2018; Received in revised form 20 October 2018; Accepted 24 October 2018
Available online 08 November 2018
0378-7753/ 

conductors (NASICON) [30–32], including $Na_{3.4}Sc_{0.4}Zr_{1.6}(SiO_4)_2(PO_4)$ (4 mS/cm) [33]. In a later work, Richards et al. studied the $Na_{10}MP_2S_{12}$ (M = Si, Ge, Sn) using first principle calculations and concluded that $Na_{10}SiP_2S_{12}$ has the highest $\sigma_{Na}$ (10.28 mS/cm) in this family of materials [31]. These authors also observed a correlation between $\sigma_{Na}$ and the ionic radius of M; the conductivity decreases as the cation radius increases, *i.e.*, $\sigma_{Na}^{Si} > \sigma_{Na}^{Ge} > \sigma_{Na}^{Sn}$. In a later work, Richards et al. synthesized the compound $Na_{10}SnP_2S_{12}$ and measured the conductivity to be 0.4 mS/cm, a value in qualitative agreement with the predicted conductivity (0.94 mS/cm) [31,34]

Recently, the Nazar and Roling groups independently discovered a new solid electrolyte, $Na_{11}Sn_2PS_{12}$ [35,36], with a structure very closely related to that of LGPS [36]. Both experimental groups fabricated single-phase $Na_{11}Sn_2PS_{12}$, a compound in a tetragonal (space group $I4_1/acd$) that facilitates wider $Na^+$ diffusion channels along the *c*-axis and in the *ab*-plane [33]. *Ab initio* simulations, conducted by the Nazar group, confirmed the three dimensional (3D) diffusion behavior of Na ions in $Na_{11}Sn_2PS_{12}$ and predicted an RT ionic conductivity of 2.4 mS/cm, a value nearly 2 times higher than the one experimentally measured (1.4 mS/cm) [36]. This discrepancy is attributed to the sluggish diffusion process that takes place at grain boundaries and the poor contact at the electrolyte-electrode interface [34].

In spite of its high conductivity, the suitability of $Na_{11}Sn_2PS_{12}$ as a solid electrolyte for SIBs has not yet been addressed. Inspired by the works of Ong et al., who investigated the phase stability, electrochemical stability, and ionic conductivity of both cationic and anionic substituted LGPS family materials [37], we examined $Na_{11}Sn_2PS_{12}$ and explored replacing Sn with Ge. For this work, we used first-principle calculations to investigate the phase and electrochemical stability of both materials. Following that, we carried out *ab initio* molecular dynamics simulations to predict the Na conductivity of $Na_{11}Ge_2PS_{12}$. Our calculations indicate an enhancement in ionic conductivity for $Na_{11}Ge_2PS_{12}$ over $Na_{11}Sn_2PS_{12}$ following an identical trend to the one found by Richards et al. in $Na_{10}MP_2S_{12}$ (M = Ge, Sn) [31]. Lastly, to understand the diffusion mechanism leading to the superior conductivity of $Na_{11}Ge_2PS_{12}$, we analyzed the Na trajectories statistically. We observed two different Na diffusion mechanisms; namely, ion hopping at lower temperatures (< 800 K) and a fluid-like distribution at higher temperatures (> 1000 K).

## 2. Computational methods

We simulated all materials using density functional theory (DFT) as implemented in the Vienna ab *initio* simulation package (VASP) [38,39]. We employed the projector augmented wave (PAW) method [40] together with the exchange-correlation described by the Perdew-Burk-Ernzerhof (PBE) functional [41] under the generalized gradient approximation (GGA) scheme. Below, we describe the specific details of each type of calculation.

### 2.1. Structure optimization

The simulation box comprises a unit cell of the $Na_{11}M_2PS_{12}$ (M = Sn, Ge), corresponding 8 formula units, i.e., $Na_{88}M_{16}P_8S_{96}$. We should note that each primitive cell has five distinct Na octahedral sites [36], see Fig. 1 (a), where two are partially occupied, and the other three are fully occupied. The partially filled positions are the Na1 (32 g with occupancy of 0.87) and the Na2 (16d with occupancy 0.78) as obtained from single crystal X-ray diffraction [36]. In the simulations, we assigned the occupancies of Na1 and Na2 to be 0.875 and 0.75, respectively. These two values were chosen to ensure compatibility with the stoichiometry and, simultaneously, keep an integer number of Na1 and Na2 atoms (we have 28 and 12 atoms for Na1 and Na2, respectively).

To determine the ground state configuration of partial occupied Na sites, we enumerated 40,000 structures and ordered all these arrangements using the electrostatic energy criterion [42] implemented in the pymatgen code [43]. First, all ions were taken to be in their idealized charge states, *i.e.*, +1 for Na, +4 for Ge and Sn, +5 for P, and −2 for S [37]. Then, 20 structures with the lowest electrostatic energies were selected for relaxation using DFT. It should be noted that various studies have also used an identical approach for the determination of the ground state structures [37,44,45].

### 2.2. Phase stability

We assessed the phase stability of $Na_{11}M_2PS_{12}$ by constructing the Na-M-P-S quaternary phase diagrams [46,47]. To better cover the phase space with as many possible compounds obtained with the above elements, we not only considered the Na-M-P-S combinations available in the Materials Project [48], but we also included compositions which have been previously obtained from related materials (*e.g.* Li/Na substitution in the Li-P-S and Li-Ge-S ternary phases [44]; O/S substitution for the Sn-P-O and Na-P-O composite [27,37]).

Consistent with the simulations carried out in the Material Project [48], all calculations were spin-polarized, and the energy was cut-off at 520 eV. Also, the Brillouin zone was sampled with 2 × 2 × 1 Gamma centered *k*-points. For the ionic relaxation, all degrees of freedom, including the lattice parameters, were optimized with an energy convergence criterion of 0.05 meV/atom. To build the phase diagram, we first computed the energy of all entries in the aforementioned Na-M-P-S phase space. Then, we constructed a four-dimensional ($\bar{E}$, $x_{Na}$, $x_M$, $x_P$) convex hull and projected it into the compositional coordinates to obtain the phase diagram. Here, $\bar{E}$ is the normalized energy per atom and $x$ is the atomic fraction of the element in the subscript with $x_S = 1 - x_{Na} - x_M - x_P$ [46,49]. To make the phase diagram readable, we further projected the constructed Na-M-P-S phase diagram into 2D ternary phase diagrams, where we chose three compounds ($Na_2S$, $P_2S_5$, and $SnS_2/GeS_2$) as the vertices of the triangles.

### 2.3. Electrochemical stability

We estimated the electrochemical stability of Na-M-P-S using two approaches: band gap and grand potential phase diagram [27,37,44]. To evaluate inherent electrochemical stability, we calculated the density of states (DOS) to obtain the material's band gap, which is also often used as an upper bound for the electrochemical window [1,50,51]. The DOS of the bulk system was carried out using the MBJ meta-GGA functional [52,53], which can give a band gap with comparable accuracy to that of hybrid functionals or the GW approximation [54–56] but with a lower computational cost [53,57].

To obtain the electrochemical stability against the electrodes, we constructed the Na grand potential phase diagram using pymatgen [27,37,44]. The grand potential phase diagram represents the Na-M-P-S system that is open to Na. Just as in a full battery, the electrolyte material is exposed to a Na reservoir at the anode side, and a Na sink at the cathode. By varying the chemical potential of Na, $\mu_{Na}$, the grand potential phase diagram can be constructed and the phase stability of the $Na_{11}M_2PS_{12}$ obtained with respect to $\mu_{Na}$ as well as the cell voltage $V|_{Na/Na^+}$. We note that $V|_{Na/Na^+} = -\mu_{Na}^{cathode}$, where $\mu_{Na}^{cathode}$ the chemical potential of Na at the cathode side [58].

Assuming Na is the only species present in the electrolyte that can be exchanged with the electrodes, the $Na_{11}M_2PS_{12}$ may undergo reduction at the anode and oxidation at the cathode. With the help of the grand potential phase diagram, one can simulate the evolution of the phase as a function of the Na chemical potential and assess whether the phases formed will influence the conductivity [37].

### 2.4. Molecular dynamics simulations

We evaluated the Na ion conductivity of $Na_{11}M_2PS_{12}$ by *ab initio*

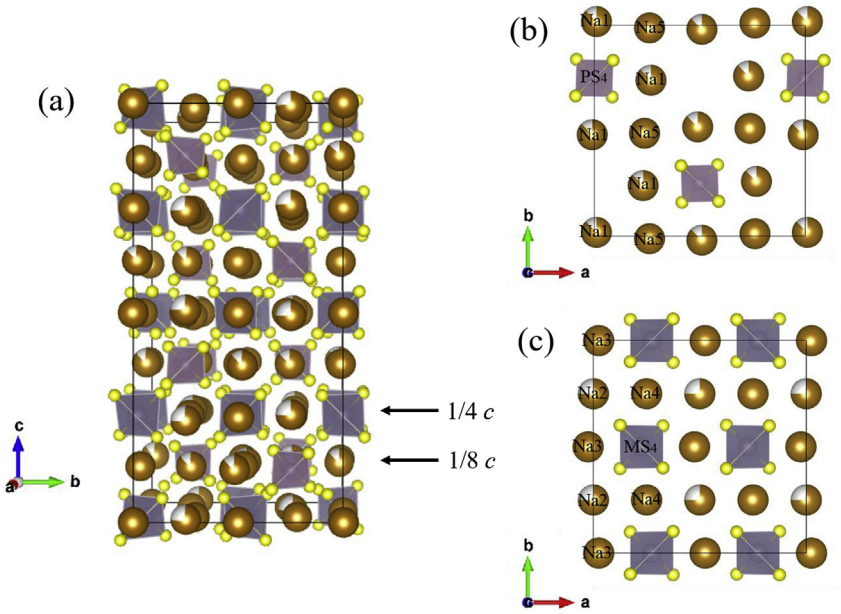


**Fig. 1.** (a) Crystal structure of $Na_{11}M_2PS_{12}$. Top view slices at (b) 1/8 *c* and (c) at 1/4 *c* are shown. 5 distinct Na sites are labeled.

molecular dynamics (AIMD) simulations. Since the Nazar group had already investigated $Na_{11}Sn_2PS_{12}$ using the AIMD method, we here only simulated $Na_{11}Ge_2PS_{12}$. Consistent with the Nazar group, the simulations were not spin-polarized, and the Brillouin zone was sampled on Γ-centered $1 \times 1 \times 1$ *k*-point grid. We set the kinetic energy cut-off at 280 eV and the energy convergence criterion for self-consistent calculations as $10^{-4}$ eV [34].

We performed the AIMD simulations in the *NVT* ensemble with a Nosé-Hoover thermostat, where the temperatures were selected to be $T = 600$ K, 700 K, 800 K, 900 K, 1000 K, and 1200 K [59,60]. The cell parameters and the initial position of atoms were identical to those obtained in the fully relaxed cells that were used to build the phase diagrams of section 2.1. For each target temperature, the total simulation time was 40 ps and the time step was set at 2 fs.

The Na self-diffusion coefficient was obtained from the mean squared displacement using the following formula [61]:

$$D_{\mathrm{Na}} = \frac{\mathrm{MSD}(\Delta t)}{6\Delta t} \tag{1}$$

where $\Delta t$ is the time interval and $\mathrm{MSD}(\Delta t)$ is the mean squared displacement of Na ions in that interval. To compute the $\mathrm{MSD}(\Delta t)$, we used the following expression [62]:

$$\mathrm{MSD}(\Delta t) = \frac{1}{N_{\mathrm{Na}}} \sum_{i=1}^{N} |\boldsymbol{r}_i(t + \Delta t) - \boldsymbol{r}_i(t)|^2 \tag{2}$$

where $N_{\mathrm{Na}}$ is the total number of Na atoms in the $Na_{11}M_2PS_{12}$ unit cell.

From the diffusion coefficient $D_{\mathrm{Na}}$, we calculated the ionic conductivity $\sigma_{\mathrm{Na}}$ through the Nernst-Einstein relation [63].

$$\sigma_{\mathrm{Na}} = \frac{(z_{\mathrm{Na}} e)^2 N_{\mathrm{Na}} D_{\mathrm{Na}}}{V k_{\mathrm{B}} T} \tag{3}$$

where $z_{\mathrm{Na}}$ is the integer charge of $Na^+$ ion ($z_{\mathrm{Na}} = +1$), $k_{\mathrm{B}}$ is the Boltzmann constant, and $V$ is the total volume of the simulation box.

The RT conductivity is obtained by Gaussian process regression (linear-basis mean with a squared exponential kernel) from the high-temperature results [64,65]. We first found the activation energy $E_a$ in the Arrhenius equation:

$$D_{\mathrm{Na}} = D^0_{\mathrm{Na}} \exp\left(-\frac{E_a}{k_{\mathrm{B}} T}\right) \tag{4}$$

where $D^0_{\mathrm{Na}}$ is a constant and (3) is then used to obtain the RT ionic conductivity. We conducted the Gaussian process for the curve fitting as implemented in MATLAB.

Based on the molecular dynamics simulations, we determined the Na jump rates among the 5 distinct sites reported in Fig. 1. Using the trajectories obtained from the AIMD simulations, we assigned the position of each Na-ion to its nearest crystallographic Na site [66]. Using the position of each Na ion in the crystal at each time step, we computed the mean jump rate

$$\tau_{\mathrm{Na}} = \frac{J}{N_{\mathrm{Na}} t} \tag{5}$$

where $J$ is the total number of jumps between two crystallographic sites and $t$ is the total simulation time. The diffusivity computed from the jump rate, $D_{\mathrm{jump}}$, can also be defined [66]:

$$D_{\mathrm{jump}} = \frac{\tau_{\mathrm{Na}} a^2}{6} \tag{6}$$

where $a$ is the distance between the Na sites in $Na_{11}Ge_2PS_{12}$, *i.e.*, $a$= 3.39 Å.

## 3. Results and discussion

### 3.1. Structure optimization and phase stability

Table 1 lists the relaxed lattice parameters obtained from the DFT

**Table 1**
The relaxed lattice parameters and phase equilibria of $Na_{11}Sn_2PS_{12}$ and $Na_{11}Ge_2PS_{12}$.

| Material | *a*(Å) | *c*(Å) | Decomposition reaction | $E_{\mathrm{hull}}$ (meV/atom) |
|---|---|---|---|---|
| $Na_{11}Sn_2PS_{12}$ | 13.763 (13.615) | 27.519 (27.224) | $Na_{11}Sn_2PS_{12} \rightleftharpoons Na_3PS_4 + 2\ Na_4SnS_4$ | 14.5 |
| $Na_{11}Ge_2PS_{12}$ | 13.551 | 27.073 | None | 0 |

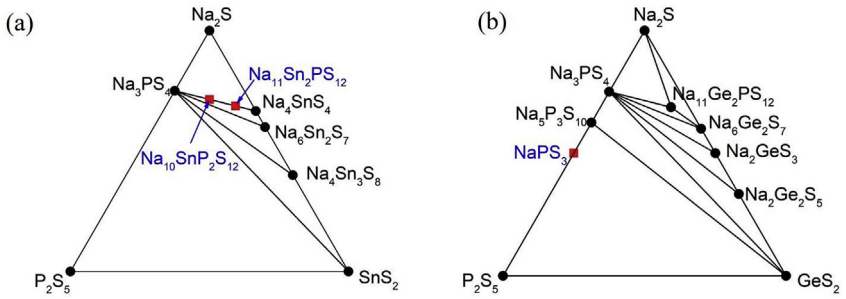


**Fig. 2.** Phase diagram of (a) $Na_{11}Sn_2PS_{12}$ and (b) $Na_{11}Ge_2PS_{12}$ calculated using the pymatgen package. Stable and unstable phases are shown using black and red dots respectively. The vertices have $E_{hull} = 0$ and the corresponding space groups are those given in the Material Project [48], i.e., $Na_2S$ ($Fm\bar{3}m$), $P_2S_5$ ($P\bar{1}$), $SnS_2$ ($P\bar{3}m1$), GeS2 ($P2_1/c$). (For interpretation of the references to colour in this figure legend, the reader is referred to the Web version of this article.)

calculations together with corresponding data from X-ray diffraction (in the brackets) [36]. The theoretical predictions and the experimental lattice parameters appear to be in good agreement. Further, due to the smaller ionic radius of Ge than Sn, the lattice parameters decrease when Ge replaces Sn. A similar trend was also observed in the LGPS family of materials [37].

The phase diagrams of both $Na_{11}Sn_2PS_{12}$ and $Na_{11}Ge_2PS_{12}$ are shown in Fig. 2, where the stable phases are denoted as black dots while the unstable phases are indicated as red squares. We observe that $Na_{11}Sn_2PS_{12}$ is unstable against the decomposition into $Na_3PS_4$ and $Na_4SnS_4$, see Fig. 2(a). Furthermore, as indicated in Table 1, $Na_{11}Sn_2PS_{12}$ shows an energy above the hull, $E_{hull}$, of 14.5 meV/atom. In contrast, $Na_{11}Ge_2PS_{12}$ is computed to be a stable phase in the Na-Ge-P-S phase space, see Fig. 2(b).

Such an $E_{hull}$ computed for $Na_{11}Sn_2PS_{12}$ is so small that, in principle, entropic contributions to the Gibbs free energy could stabilize this material [37]. Additionally, $Na_{10}SnP_2S_{12}$ appears to be more unstable (or more difficult to synthesize) than $Na_{11}Sn_2PS_{12}$, see Fig. 2 (a), with a calculated energy above hull of 18.05 meV/atom. We should also stress that $Na_{10}SnP_2S_{12}$ and $Na_{11}Sn_2PS_{12}$ lie along the same line connecting $Na_3PS_4$ and $Na_4SnS_4$, suggesting that both materials have similar decomposition products.

To further verify the phase stability of $Na_{11}Sn_2PS_{12}$ and $Na_{11}Ge_2PS_{12}$, we also considered their reaction energy, $\Delta E$, which is defined as the difference between products and reactants ground state energies. Starting from the precursors, *i.e.*, $Na_2S$, $P_2S_5$, Sn(Ge)$S_2$ [36], the reactions can be written as follows

$$5.5\,Na_2S + 2\,SnS_2 + 0.5\,P_2S_5 \rightarrow Na_{11}Sn_2PS_{12} \quad (7a)$$

$$5.5\,Na_2S + 2\,GeS_2 + 0.5\,P_2S_5 \rightarrow Na_{11}Ge_2PS_{12} \quad (7b)$$

Consistent with the phase diagram results discussed above, the synthesis of $Na_{11}Ge_2PS_{12}$ appears to be more favorable than that of $Na_{11}Sn_2PS_{12}$.

### 3.2. Band gap

The densities of states of both $Na_{11}Sn_2PS_{12}$ and $Na_{11}Ge_2PS_{12}$ are reported in Fig. 3. The band gap, defined as the energy difference between the valence band maximum and the conduction band minimum, was calculated to be 1.80 eV for $Na_{11}Sn_2PS_{12}$ and 2.87 eV for $Na_{11}Ge_2PS_{12}$. As explained earlier, the band gap of the material provides an upper limit for the electrochemical window [51]. The substitution of Sn with Ge significantly increases the band gap, suggesting a wider electrochemical window for $Na_{11}Ge_2PS_{12}$. Also, the predicted bandgap of $Na_{11}Ge_2PS_{12}$ falls with the range of voltages characteristic of various Na-ion cathodes and Na-S batteries (1.78–2.08 V) [67–69]. These results suggest that $Na_{11}Ge_2PS_{12}$ could be used in Na batteries characterized by a moderate voltage, *e.g.*, Na-S [69].

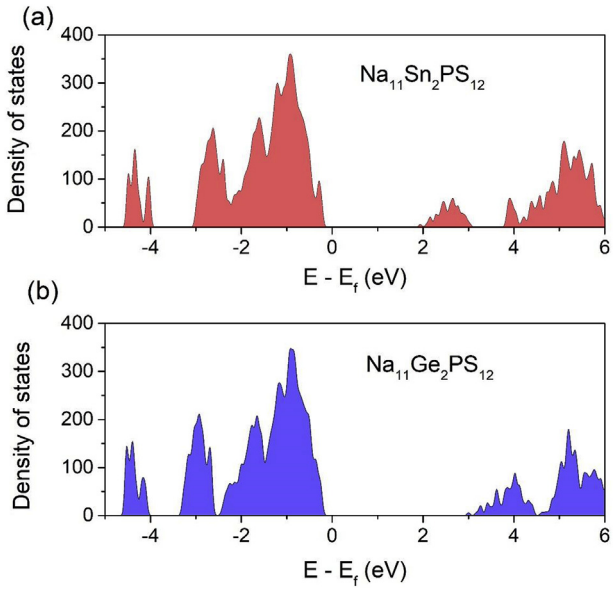


**Fig. 3.** Calculated density of states for (a) $Na_{11}Sn_2PS_{12}$ and (b) $Na_{11}Ge_2PS_{12}$. The Fermi level $E_f$ is shifted to 0 eV.

### 3.3. Electrochemical stability against electrodes

A good electrochemical compatibility between the electrolyte and the electrode is essential for high capacity retention and low impedance. In a fully charged battery, the electrolyte may undergo reduction at the anode or oxidation at the cathode to form a passivating solid electrolyte interphase (SEI). Such an SEI layer is crucial since it may prevent further decomposition of the electrolyte and reduce the overpotential and concentration polarization [70]. Interestingly, this approach has been successful in predicting reduction products of LGPS in a Li/LGPS/LGPS-C cell [71,72].

To check the possible phases in the SEI layer, we constructed the grand potential phase diagram. Fig. 4 shows the phase and possible decomposition products resulting from applying a voltage (*vs.* $Na/Na^+$) to $Na_{11}M_2PS_{12}$. The electrochemical stability window is determined by the range of voltages at which the $Na_{11}M_2PS_{12}$ phase is stable, *i.e.*, the phase is a vertex of the convex hull. Interestingly, $Na_{11}Ge_2PS_{12}$ has a narrower electrochemical stability window than $Na_{11}Sn_2PS_{12}$.

Both materials are reduced below 1.15–1.16 V, where $Na_{11}Sn_2PS_{12}$ decomposes into $Na_3PS_4$ and $Na_4SnS_4$, see Table 1. Further decreasing the voltage triggers multiple thermodynamic voltage plateaus that correspond to the Na-P and Na-Ge/Na-Sn alloying processes [37]. Conversely, the electrolytes are oxidized as a consequence of Na extraction by increasing the voltage, *i.e.*, lowering the $\mu_{Na}$.

Despite the narrow electrochemical window, we should note that $Na_2S$, $N_3S$, and other Na-Ge/Na-Sn alloys, which are expected to be Na

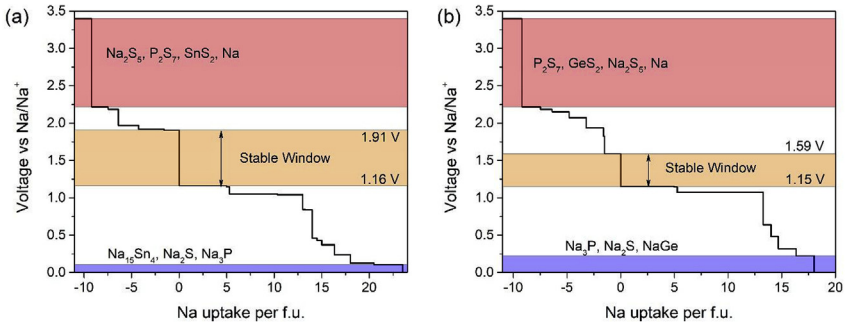


**Fig. 4.** Voltage of (a) $Na_{11}Sn_2PS_{12}$ and (b) $Na_{11}Ge_2PS_{12}$ with respect to the Na uptake and extraction processes at various Na chemical potentials. The equilibria phases at the anode and cathode are denoted with red and blue. The stable window is in orange. (For interpretation of the references to colour in this figure legend, the reader is referred to the Web version of this article.)

ion conductors [18,73], are formed at the low voltages (anode side). When the voltage is sufficiently high (cathode side), $Na_{11}M_2PS_{12}$ is oxidized and decomposes into $Na_3PS_4$, a well-known Na ion conductor with a $\sigma_{Na}$ at RT of $\sim 10^{-1}$ mS/cm [18]. Consequently, the phases formed at both the anode and cathode likely act as SEI layers between the electrolyte and the electrodes, preventing further decomposition of the electrolyte and effectively enlarging the electrochemical window.

### 3.4. Na diffusivity and conductivity

The Na ionic conductivity is one crucial factor in the battery performance. The self-diffusion coefficient calculated with (1) is shown in Fig. 5, together with the $Na_{11}Sn_2PS_{12}$ data retrieved from the literature [36]. The logarithm of $D$ was fitted against $1/T$ following the Arrhenius equation (4). The activation energy, $E_a$, decreases by replacing Sn with Ge. A similar trend has also been observed for $Na_{10}MP_2S_{12}$ (M = Ge, Sn) [74], a material for which $E_a$ increases with the ionic radius of M.

Using Gaussian process regression, the RT ionic conductivity for $Na_{11}Ge_2PS_{12}$ is predicted to be 4.7 mS/cm, two times higher than that of $Na_{11}Sn_2PS_{12}$ (2.1 mS/cm). We report in Fig. 6 the $\sigma_{Na}$ at RT and corresponding $E_a$ of a number of NASICON-type electrolytes [17,18,24,29,35,36,74–77]. We should stress that $Na_{11}Ge_2PS_{12}$ is in the superionic conductivity region ($\sigma_{Na} \geq 1$ mS/cm) [35] and it is characterized by a remarkably low $E_a$. Additionally, $Na_{11}Ge_2PS_{12}$ is superior to many other reported SSEs, including $Na_3SbS_4$ [77], $Na_{10}GeP_2S_{12}$ [74], $Na_{11}Sn_2PS_{12}$ [35].

### 3.5. Na ion diffusion mechanism

To gain more insight into the Na diffusion mechanism in $Na_{11}Ge_2PS_{12}$, we analyzed the AIMD trajectories. First, we calculated the Na ion probability density $P(\boldsymbol{r})$ [66], a quantity that can be used to find the areas where Na atoms are more frequently found [13]. By voxelating uniformly the computational domain, $P(\boldsymbol{r})$ is estimated by averaging the number of Na ions in each voxel over the total simulation timescale [44]. As an example, we show the Na ion probability density for $Na_{11}Ge_2PS_{12}$ at 1000 K, a value close to the synthesis temperature

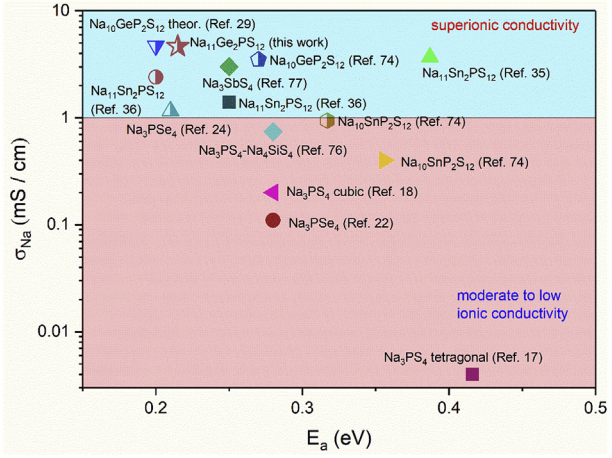


**Fig. 6.** Na ionic conductivity and the activation energy for a variety of electrolytes. The common conductivity threshold (1 mS/cm) separates the region for superionic conductivity in light blue and low ionic conductivity in pink. Solid symbols represent values from experimental work, while half open symbols correspond to theoretical predictions. The red star denotes $Na_{11}Ge_2PS_{12}$. (For interpretation of the references to colour in this figure legend, the reader is referred to the Web version of this article.)

(700 °C) of $Na_{11}Sn_2PS_{12}$ [36]. In Fig. 7, we can clearly see a 3D network connecting both the *ab*-plane and the *c*-axis, consistent with previously reported pathways for $Na_{11}Sn_2PS_{12}$ [36]. In contrast to the diffusion behavior of LGPS-like materials which favor the diffusion along the *c*-axis, diffusion in the *ab*-plane of $Na_{11}Ge_2PS_{12}$ is computed to be faster than that along the c-axis, see Fig. 5(b). This may be due to the wider diffusion channels present in the *ab*-plane of $Na_{11}Ge_2PS_{12}$ compared to those found in LGPS-like materials [74]. Also in Fig. 5(b), we observe that the diffusivity along the *c*-axis does not change significantly if $T < 800$ K, suggesting that the diffusion along the *c*-axis is promoted particularly at a sufficiently high temperature.

Using the method described in section 2.4, we calculated the jump

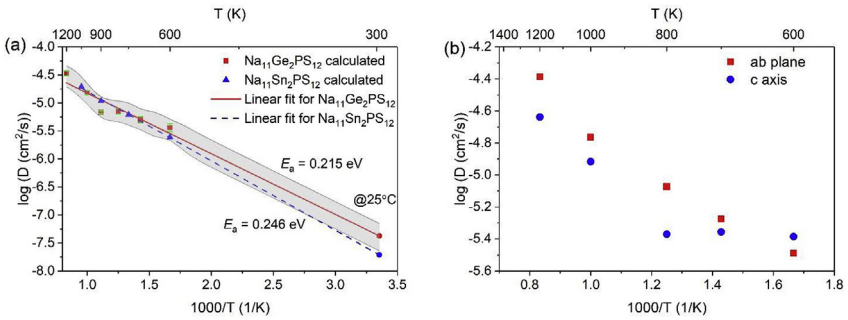


**Fig. 5.** (a) Logarithm diffusivity computed for $Na_{11}Sn_2PS_{12}$ and $Na_{11}Ge_2PS_{12}$ as a function of the inverse of the temperature. The grey area corresponds to a 95% credibility interval. (b) The diffusivity in the *ab*-plane and along the *c*-axis for $Na_{11}Ge_2PS_{12}$ at the computed temperatures.

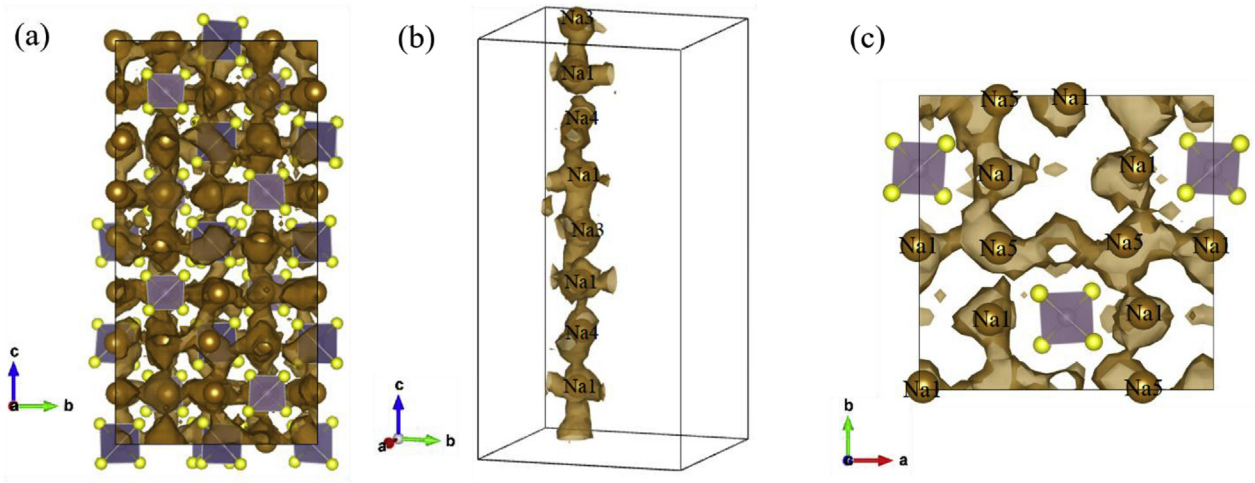


**Fig. 7.** (a) Na probability density distribution in $Na_{11}Ge_2PS_{12}$ at 1000 K. (b) Projections along the *c*-axis and (c) along the *ab*-plane at 1/8 *c*.

**Table 2**
Mean jump rates for the Na ion transition between different Na crystallographic sites at 1000 K, in the unit (0.01 jumps/ps). Every entry corresponds to a jump starting from the site in the column and ending at the site indicated by its row.

| | Na1 | Na2 | Na3 | Na4 | Na5 |
|---|---|---|---|---|---|
| Na1 | 61.14 | 0.00 | 4.32 | 3.84 | 8.30 |
| Na2 | 0.00 | 44.86 | 4.29 | 5.00 | 0.00 |
| Na3 | 4.63 | 4.03 | 55.34 | 0.00 | 0.00 |
| Na4 | 3.69 | 5.14 | 0.00 | 51.53 | 0.00 |
| Na5 | 8.13 | 0.00 | 0.00 | 0.00 | 26.39 |

rates of Na ions between different crystallographic positions. As listed in Table 2, every entry represents a jump starting from the site in the given column and ending at the site in the corresponding row, *e.g.*, the jump rate for Na1→Na4 is $3.84 \times 10^{-2}$ $ps^{-1}$. The most striking observation is the much higher jump rates between identical sites, such as Na1→Na1, than those for different sites, such as Na2→Na4. Such a phenomenon is the opposite of the one encountered in the Na diffusion in $Na_3PS_4$, where the hops between identical sites are orders of magnitude lower than the jumps between different type of sites [34]. We also note that certain hops appear not to happen, such as Na1→Na2 and Na5→Na3. This may be explained by looking at the structure of $Na_{11}Ge_2PS_{12}$ in Fig. 1(a) and (b), where Na1/Na5 and Na2/Na3 are in different layers along the *c* axis. Therefore, the distance between those sites is two times larger than that found for neighboring sites in the *ab*-plane.

To distinguish the jump rate contributions originating from either the *ab*-plane or the *c*-axis hops, we subdivided the jumps into the two categories as shown in Table 3. As expected, the rates in the *ab*-plane are higher than those along the *c*-axis, in agreement with the self-diffusivity results reported in Fig. 5(b).

Despite the high jump rates, it is highly probable that a Na ion returns to its original site after hopping to a neighboring site, making no contributions to the macroscopic diffusion. Since only useful jumps cause macroscopic diffusion [34], we investigated sequentially two continuous jumps and excluded the back-and-forth hops to obtain the net rates. The diffusivity calculated using (6) is $5.41 \times 10^{-9}$ m [2]/s at 1000 K. This value is in quantitative agreement with the one derived from (1), i.e., $1.55 \times 10^{-9}$ m [2]/s.

**Table 3**
Mean jump rates along *c*-axis and in the *ab*-plane as well as net jump rates for the Na ion transition between identical Na sites at 1000 K, in the unit (0.01 jumps/ps).

| | Na1→Na1 | Na2→Na2 | Na3→Na3 | Na4→Na4 | Na5→Na5 |
|---|---|---|---|---|---|
| *c*-axis | 0.00 | 15.48 | 15.74 | 13.18 | 0.00 |
| *ab*-plane | 61.14 | 29.38 | 39.60 | 38.35 | 26.39 |
| Net jump | 17.36 | 10.88 | 12.36 | 20.34 | 2.10 |

We also conducted the van Hove correlation analysis for $Na_{11}Ge_2PS_{12}$ to understand the Na diffusion mechanism at different temperatures. The self-part of the van Hove correlation is a function of the radial distance $r$ and the time $t$, following formula [78].

$$G_s(r, t) = \frac{1}{4\pi r^2 N_{Na}} \sum_{i=1}^{N_{Na}} \delta\left[r - |\boldsymbol{r}_i(t_0) - \boldsymbol{r}_i(t + t_0)|\right]_{t_0} \quad (8)$$

where $\delta(\cdot)$ is the Dirac distribution, and the angle brackets denote the ensemble average starting from an initial time $t_0$. Given $r$ and $t$, $G_s(r, t)$ indicates the probability of finding one Na ion at $r$ in the time interval $[t_0, t]$ [78].

Fig. 8 shows the self-part of the van Hove correlation as a function of radial distance $r$ and time $t$ at various temperatures. As suggested by the Islam group [78], the first peak near $r$= 1 Å corresponds to the typical atomic vibrations around equilibrium positions. We also notice a second peak at ~4 Å, see Fig. 8(a) and (b), which is related to the Na hopping process because the peak position equals just the average distance between neighbor sites in $Na_{11}Ge_2PS_{12}$. The second peak around 4 Å is clearly visible at moderate computational time scales. At higher temperatures, the intensity of the first peak decreases, eventually vanishing after a period of time, *e.g.*, $t$= 30 ps, see Fig. 8(d), suggesting that the Na ions migrate from their initial positions. Further, the second peak cannot be clearly identified, and the curves have a much longer tail if $t$ and $T$ increase, see Fig. 8(c) and (d). If $T$> 1200 K and $t$> 10 ps, the $G_s(r, t)$ does not display any prominent peaks, suggesting a fluid-like distribution of Na ions.

## 4. Conclusion

We studied the $Na_{11}M_2PS_{12}$ (M = Sn, Ge) family of materials and investigated their phase and electrochemical stability, together with their conductivity using first principle calculations. Our simulations show that, while $Na_{11}Sn_2PS_{12}$ is only metastable, $Na_{11}Ge_2PS_{12}$ is stable with zero energy above the hull. The computed DOS indicates that both materials are semiconductors with a band gap of 1.80 eV and 2.87 eV for $Na_{11}Sn_2PS_{12}$ and $Na_{11}Ge_2PS_{12}$, respectively. Both materials display a relatively narrow electrochemical stability window. However, the decomposed phases could act as SEI layers to prevent further electrolyte decomposition and ensure sufficient conductivity.

We also carried out *ab initio* molecular dynamics simulations on $Na_{11}Ge_2PS_{12}$ to predict its conductivity and study the diffusion

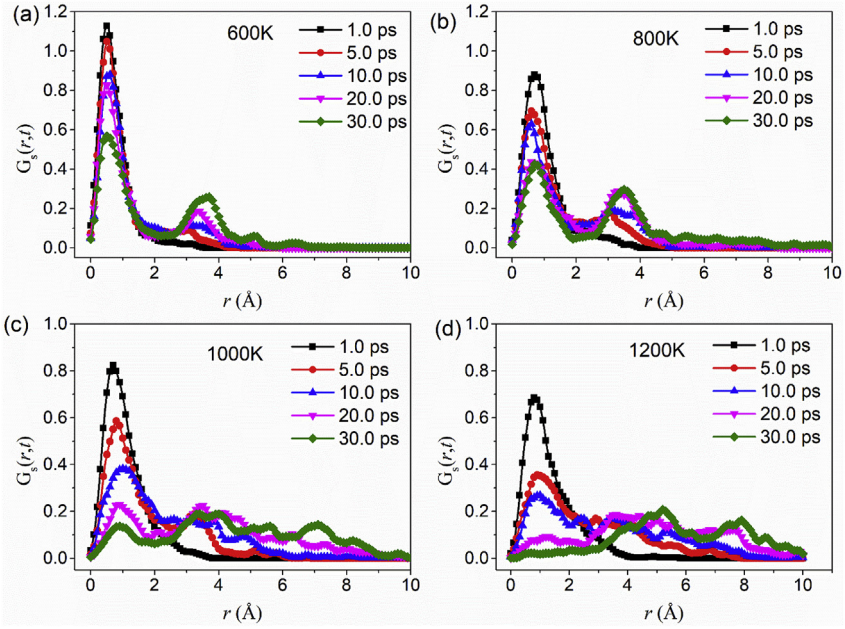


**Fig. 8.** Self-part of the van Hove correlation function for $Na_{11}Ge_2PS_{12}$ at (a) 600 K, (b) 800 K, (c) 1000 K, (d) 1200 K. Five different time scales, $t$ = 1 ps, 5 ps, 10 ps, 20 ps, 30 ps, are illustrated for each temperature to see the evolution of the correlation.

mechanism. The simulations indicate an RT conductivity of 4.7 mS/cm, a value two times higher than that of $Na_{11}Sn_2PS_{12}$ and even comparable to that of the best NASICON-type solid electrolytes. The high conductivity may be attributed to the 3D diffusional pathways encountered in $Na_{11}Ge_2PS_{12}$. Na hopping is favored along the *ab*-plane compared to the *c*-axis. Further analysis indicates that Na hops occur more frequently between identical Na sites and that jumps in the *ab*-plane are preferred.

## Conflicts of interest

There is no conflict of interest to declare.

## Acknowledgment

The authors gratefully acknowledge the Research Grants Council of Hong Kong for support through the projects (16207615, 16227016, and 16204517), the Guangzhou Science and Technology Program (No. 2016201604030020), the Science and Technology Planning Project of Guangdong Province, China (No. 2016A050503042), and the Science and Technology Program of Nansha District (No. 2015CX009). Mohammed B. Effat acknowledges the support of the Research Grants Council through the Hong Kong PhD Fellowship Scheme.

## Appendix A. Supplementary data

Supplementary data to this article can be found online at https://doi.org/10.1016/j.jpowsour.2018.10.077.

## References

[1] Z. Lu, F. Ciucci, Chem. Mater. 29 (2017) 9308–9319.
[2] Y. Xie, Y. Dall'Agnese, M. Naguib, Y. Gogotsi, M.W. Barsoum, H.L. Zhuang, P.R. Kent, ACS Nano 8 (2014) 9606–9615.
[3] D. Aurbach, G.S. Suresh, E. Levi, A. Mitelman, O. Mizrahi, O. Chusid, M. Brunelli, Adv. Mater. 19 (2007) 4260–4267.
[4] D. Aurbach, Z. Lu, A. Schechter, Y. Gofer, H. Gizbar, R. Turgeman, Y. Cohen, M. Moshkovich, E. Levi, Nature 407 (2000) 724.
[5] A.L. Lipson, B. Pan, S.H. Lapidus, C. Liao, J.T. Vaughey, B.J. Ingram, Chem. Mater. 27 (2015) 8442–8447.
[6] D. Er, J. Li, M. Naguib, Y. Gogotsi, V.B. Shenoy, ACS Appl. Mater. Interfaces 6 (2014) 11173–11179.
[7] M.-C. Lin, M. Gong, B. Lu, Y. Wu, D.-Y. Wang, M. Guan, M. Angell, C. Chen, J. Yang, B.-J. Hwang, Nature 520 (2015) 324.
[8] S.W. Kim, D.H. Seo, X. Ma, G. Ceder, K. Kang, Advanced Energy Materials 2 (2012) 710–721.
[9] N. Yabuuchi, K. Kubota, M. Dahbi, S. Komaba, Chem. Rev. 114 (2014) 11636–11682.
[10] H. Pan, Y.-S. Hu, L. Chen, Energy Environ. Sci. 6 (2013) 2338–2360.
[11] M.D. Slater, D. Kim, E. Lee, C.S. Johnson, Adv. Funct. Mater. 23 (2013) 947–958.
[12] M. Armand, J.-M. Tarascon, Nature 451 (2008) 652.
[13] Y. Wang, W.D. Richards, S.P. Ong, L.J. Miara, J.C. Kim, Y. Mo, G. Ceder, Nat. Mater. 14 (2015) 1026.
[14] K. Takada, Acta Mater. 61 (2013) 759–770.
[15] J. Kang, B. Han, J. Phys. Chem. Lett. 7 (2016) 2671–2675.
[16] J. Kang, H. Chung, C. Doh, B. Kang, B. Han, J. Power Sources 293 (2015) 11–16.
[17] A. Hayashi, K. Noi, N. Tanibata, M. Nagao, M. Tatsumisago, J. Power Sources 258 (2014) 420–423.
[18] A. Hayashi, K. Noi, A. Sakuda, M. Tatsumisago, Nat. Commun. 3 (2012) 856.
[19] Z. Zhang, Y. Shao, B. Lotsch, Y.-S. Hu, H. Li, J. Janek, L.F. Nazar, C.-W. Nan, J. Maier, M. Armand, L. Chen, Energy Environ. Sci. (2018) 1945–1976.
[20] R.P. Rao, H. Chen, L.L. Wong, S. Adams, J. Mater. Chem. 5 (2017) 3377–3388.
[21] M. Tatsumisago, A. Hayashi, Int. J. Appl. Glass Sci. 5 (2014) 226–235.
[22] S.-H. Bo, Y. Wang, G. Ceder, J. Mater. Chem. 4 (2016) 9044–9053.
[23] Z. Yu, S.L. Shang, J.H. Seo, D. Wang, X. Luo, Q. Huang, S. Chen, J. Lu, X. Li, Z.K. Liu, Adv. Mater. 29 (2017) 1605561.
[24] L. Zhang, K. Yang, J. Mi, L. Lu, L. Zhao, L. Wang, Y. Li, H. Zeng, Advanced Energy Materials 5 (2015) 1501294.
[25] N. Kamaya, K. Homma, Y. Yamakawa, M. Hirayama, R. Kanno, M. Yonemura, T. Kamiyama, Y. Kato, S. Hama, K. Kawamoto, Nat. Mater. 10 (2011) 682.
[26] R. Kanno, M. Murayama, J. Electrochem. Soc. 148 (2001) A742–A746.
[27] Y. Mo, S.P. Ong, G. Ceder, Chem. Mater. 24 (2011) 15–17.
[28] P. Bron, S. Johansson, K. Zick, J. r. Schmedt auf der Günne, S. Dehnen, B. Roling, J. Am. Chem. Soc. 135 (2013) 15694–15697.
[29] V.S. Kandagal, M.D. Bharadwaj, U.V. Waghmare, J. Mater. Chem. 3 (2015) 12992–12999.
[30] Y. Deng, C. Eames, L.H. Nguyen, O. Pecher, K.J. Griffith, M. Courty, B. Fleutot, J.-N. Chotard, C.P. Grey, M.S. Islam, Chem. Mater. 30 (2018) 2618–2630.
[31] Y. Li, Z. Deng, J. Peng, E. Chen, Y. Yu, X. Li, J. Luo, Y. Huang, J. Zhu, C. Fang, Chemistry–A European Journal 24 (2018) 1057–1061.
[32] Z. Yu, S.-L. Shang, Y. Gao, D. Wang, X. Li, Z.-K. Liu, D. Wang, Nanomater. Energy 47 (2018) 325–330.
[33] Q. Ma, M. Guin, S. Naqash, C.-L. Tsai, F. Tietz, O. Guillon, Chem. Mater. 28 (2016) 4821–4828.
[34] N.J.J. de Klerk, M. Wagemaker, Chem. Mater. 28 (2016) 3122–3130.
[35] M. Duchardt, U. Ruschewitz, S. Adams, S. Dehnen, B. Roling, Angew. Chem. Int. Ed. 57 (2018) 1351–1355.
[36] Z. Zhang, E. Ramos, F. Lalère, A. Assoud, K. Kaup, P. Hartman, L.F. Nazar, Energy Environ. Sci. 11 (2018) 87–93.
[37] S.P. Ong, Y. Mo, W.D. Richards, L. Miara, H.S. Lee, G. Ceder, Energy Environ. Sci. 6 (2013) 148–156.
[38] G. Kresse, J. Furthmüller, Phys. Rev. B 54 (1996) 11169.
[39] G. Kresse, J. Furthmüller, Comput. Mater. Sci. 6 (1996) 15–50.

[40] P.E. Blöchl, Phys. Rev. B 50 (1994) 17953.
[41] J.P. Perdew, K. Burke, M. Ernzerhof, Phys. Rev. Lett. 77 (1996) 3865.
[42] P.P. Ewald, Ann. Phys. 369 (1921) 253–287.
[43] S.P. Ong, W.D. Richards, A. Jain, G. Hautier, M. Kocher, S. Cholia, D. Gunter, V.L. Chevrier, K.A. Persson, G. Ceder, Comput. Mater. Sci. 68 (2013) 314–319.
[44] Z. Deng, Z. Zhu, I.-H. Chu, S.P. Ong, Chem. Mater. 29 (2016) 281–288.
[45] K. Oh, D. Chang, B. Lee, D.-H. Kim, G. Yoon, I. Park, B. Kim, K. Kang, Chem. Mater. 30 (2018) 4995–5004.
[46] S. Ping Ong, L. Wang, B. Kang, G. Ceder, Chem. Mater. 20 (2008) 1798–1807.
[47] S.P. Ong, A. Jain, G. Hautier, B. Kang, G. Ceder, Electrochem. Commun. 12 (2010) 427–430.
[48] A. Jain, S.P. Ong, G. Hautier, W. Chen, W.D. Richards, S. Dacek, S. Cholia, D. Gunter, D. Skinner, G. Ceder, Apl. Mater. 1 (2013) 011002.
[49] C.B. Barber, D.P. Dobkin, H. Huhdanpaa, ACM Trans. Math Software 22 (1996) 469–483.
[50] Z. Lu, F. Ciucci, J. Mater. Chem. 6 (2018) 5185–5192.
[51] S.P. Ong, O. Andreussi, Y. Wu, N. Marzari, G. Ceder, Chem. Mater. 23 (2011) 2979–2986.
[52] A.D. Becke, E.R. Johnson, AIP, Editon edn., 2006.
[53] F. Tran, P. Blaha, Phys. Rev. Lett. 102 (2009) 226401.
[54] M. Shishkin, M. Marsman, G. Kresse, Phys. Rev. Lett. 99 (2007) 246403.
[55] M. Shishkin, G. Kresse, Phys. Rev. B 74 (2006) 035101.
[56] M. Shishkin, G. Kresse, Phys. Rev. B 75 (2007) 235102.
[57] D. Koller, F. Tran, P. Blaha, Phys. Rev. B 83 (2011) 195134.
[58] A. Urban, D.-H. Seo, G. Ceder, npj Computational Materials 2 (2016).
[59] S. Nosé, J. Chem. Phys. 81 (1984) 511–519.
[60] W.G. Hoover, Phys. Rev. 31 (1985) 1695.
[61] A. Einstein, Ann. Phys. 322 (1905) 549–560.
[62] X. He, Y. Zhu, A. Epstein, Y. Mo, npj Computational Materials 4 (2018).
[63] P. Heitjans, S. Indris, J. Phys. Condens. Matter 15 (2003) R1257.
[64] C.E. Rasmussen, Advanced Lectures on Machine Learning, Editon edn., Springer, 2004, pp. 63–71.
[65] A. O'Hagan, J.F.C. Kingman, J. Health.com the Royal Statistical Society. Series B (Methodological), (1978), pp. 1–42.
[66] C. Chen, Z. Lu, F. Ciucci, Sci. Rep. 7 (2017) 40769.
[67] W. Li, M. Zhou, H. Li, K. Wang, S. Cheng, K. Jiang, Energy Environ. Sci. 8 (2015) 2916–2921.
[68] Y. Liu, N. Zhang, L. Jiao, Z. Tao, J. Chen, Adv. Funct. Mater. 25 (2015) 214–220.
[69] S. Xin, Y.X. Yin, Y.G. Guo, L.J. Wan, Adv. Mater. 26 (2014) 1261–1265.
[70] C. Liu, Z.G. Neale, G. Cao, Mater. Today 19 (2016) 109–123.
[71] F. Han, Y. Zhu, X. He, Y. Mo, C. Wang, Advanced Energy Materials 6 (2016) 1501590.
[72] F. Han, T. Gao, Y. Zhu, K.J. Gaskell, C. Wang, Adv. Mater. 27 (2015) 3473–3483.
[73] H.K. Patel, S.W. Martin, Phys. Rev. B 45 (1992) 10292.
[74] W.D. Richards, T. Tsujimura, L.J. Miara, Y. Wang, J.C. Kim, S.P. Ong, I. Uechi, N. Suzuki, G. Ceder, Nat. Commun. 7 (2016) 11009.
[75] S.-H. Bo, Y. Wang, J.C. Kim, W.D. Richards, G. Ceder, Chem. Mater. 28 (2015) 252–258.
[76] N. Tanibata, K. Noi, A. Hayashi, M. Tatsumisago, RSC Adv. 4 (2014) 17120–17123.
[77] L. Zhang, D. Zhang, K. Yang, X. Yan, L. Wang, J. Mi, B. Xu, Y. Li, Advanced science 3 (2016) 1600089.
[78] Y. Deng, C. Eames, B. Fleutot, R. David, J.N. Chotard, E. Suard, C. Masquelier, M.S. Islam, ACS Appl. Mater. Interfaces 9 (2017) 7050–7058.